Isovector and isoscalar dipole excitations in [9]Be and [10]Be studied with antisymmetrized molecular dynamics

AUTHOR(S):

Kanada-En'yo, Yoshiko

CITATION:

Kanada-En'yo, Yoshiko. Isovector and isoscalar dipole excitations in [9]Be and [10]Be studied with antisymmetrized molecular dynamics. Physical Review C - Nuclear Physics 2016, 93(2): 024322.

ISSUE DATE:

2016-02-29

URL:

http://hdl.handle.net/2433/218373

PHYSICAL REVIEW C **93**, 024322 (2016)

Isovector and isoscalar dipole excitations in ^{9}Be and ^{10}Be studied with antisymmetrized molecular dynamics

Yoshiko Kanada-En'yo
Department of Physics, Kyoto University, Kyoto 606-8502, Japan
(Received 26 November 2015; revised manuscript received 23 January 2016; published 29 February 2016)

Isovector and isoscalar dipole excitations in ^{9}Be and ^{10}Be are investigated in the framework of antisymmetrized molecular dynamics, in which angular-momentum and parity projections are performed. In the present method, 1p-1h excitation modes built on the ground state and a large amplitude α-cluster mode are taken into account. The isovector giant dipole resonance (GDR) in $E > 20$ MeV shows the two-peak structure, which is understood from the dipole excitation in the 2α core part with the prolate deformation. Because of valence neutron modes against the 2α core, low-energy $E1$ resonances appear in $E < 20$ MeV, exhausting about 20% of the Thomas-Reiche-Kuhn sum rule and 10% of the calculated energy-weighted sum. The dipole resonance at $E \sim 15$ MeV in ^{10}Be can be interpreted as the parity partner of the ground state having a ^{6}He $+\alpha$ structure and has remarkable $E1$ strength because of the coherent contribution of two valence neutrons. The isoscalar dipole strength for some low-energy resonances is significantly enhanced by the coupling with the α-cluster mode. For the $E1$ strength of ^{9}Be, the calculation overestimates the energy-weighted sum (EWS) in the low-energy ($E < 20$ MeV) and GDR ($20 < E < 50$ MeV) regions by a factor of 1.6 and underestimates the width of the GDR, whereas it reasonably describes the GDR energy and also the ratio of the EWS in the low-energy region to that of the GDR region.

DOI: 10.1103/PhysRevC.93.024322

I. INTRODUCTION

In neutron-rich nuclei, various exotic phenomena appear because of excess neutrons. One of the current issues concerning exotic excitation modes in neutron-rich nuclei is low-energy dipole excitations [1–77]. For stable nuclei, isovector giant dipole resonances (GDRs) have been systematically observed in various nuclei by measurements of photonuclear cross sections (for example, see Ref. [78] and references therein). The GDR is understood as an opposite oscillation between protons and neutrons and microscopically described by coherent 1p-1h excitations. Peak structure of the strength function of the GDR has been often discussed in relation to nuclear deformation. In neutron-rich nuclei, low-energy dipole resonances have been suggested to appear because of excess neutron motion against a core. The so-called soft dipole resonance, which is the enhanced $E1$ strength observed in the extremely low-energy ($E \leqslant$ 2–3 MeV) region in neutron halo nuclei such as ^{6}He and ^{11}Li, has been intensively studied by experimental and theoretical groups and often discussed in relation to the two-neutron correlation [1–8,13–30]. More generally the low-energy $E1$ strength typically in the $5 \leqslant E \leqslant$ 15 MeV region is predicted in various nuclei in a wide mass region, and the one decoupled from the GDR is called the pigmy dipole resonance. The role of excess neutrons and the collectivity of these low-energy dipole excitations are topics of interest in theoretical studies. The low-energy $E1$ strength has been also discussed in relation to neutron skin thickness and the density dependence of the symmetry energy, though their correlation is under debate [46,48,60–63,72,77].

The experimental measurements of the low-energy $E1$ strength in ^{9}Be by photodisintegration have been performed mainly for astrophysical interests [79–83]. In recent years, precise data of the $E1$ strength for low-lying positive-parity states of ^{9}Be have been reported [83]. Moreover, the recently measured photodisintegration cross sections of ^{9}Be indicate the significant low-energy $E1$ strength around $E = 10$ MeV exhausting about 10% of the Thomas-Reiche-Kuhn (TRK) sum rule [84], consistent with the bremsstrahlung data [81]. The experimental data of the $E1$ strength of ^{9}Be are available in a wide energy region from low energy to high energy: the $E1$ strength for the positive-parity states in $E \leqslant$ 5 MeV [83], the significant $E1$ strength around $E = 10$ MeV [81,84], and the $E1$ strength in $E > 20$ MeV for the GDR [85].

Our aim is to investigate isovector and isoscalar dipole strengths in ^{9}Be and ^{10}Be to understand the low-energy dipole modes. I try to clarify the role of excess neutrons and the decoupling mechanism of the low-energy dipole modes from the GDR. The low-lying states of ^{9}Be are understood by $2\alpha + n$ cluster structures as discussed in cluster models [86–90]. The photodisintegration cross sections in the very low-energy region of ^{9}Be have been theoretically investigated by two-body (^{8}Be $+n$) and three-body ($2\alpha + n$) cluster models with continuum states [91–97]. However, such cluster models are not able to describe the high-energy dipole strength of the GDR, to which coherent 1p-1h excitations may contribute. To investigate the pygmy and giant dipole resonances in general nuclei, shell model and mean-field approaches were applied. The former may not be suitable for such largely deformed nuclei as Be isotopes having cluster structures. The latter is usually based on the random phase approximation (RPA) with and without continuum. Although the RPA calculation is successful for a variety of collective excitations in heavy mass nuclei, it is a small amplitude approximation neglecting large amplitude motion. Moreover, in most current mean-field approaches, the RPA calculation is based on a parity-symmetric mean field in a strong coupling picture without the angular-momentum and parity projections, and the coupling of single-particle excitations in the mean field with rotation and parity transformation is not taken into account microscopically.

To take into account the coherent 1p-1h excitations and the large amplitude cluster mode as well as the angular-momentum and parity projections, we develop a method of antisymmetrized molecular dynamics (AMD) [98–103]. The time-dependent AMD, which was originally developed for study of heavy-ion reactions [98,99], was applied to investigate $E1$ and monopole excitations [39,104]. However, in the time-dependent AMD approach, the angular-momentum and parity projections are not performed, and, therefore, ground state structures and the coupling of single-particle excitations with the rotational motion are not sufficiently described. Instead of the time-dependent AMD, we superpose the angular-momentum and parity-projected wave functions of various configurations including the 1p-1h and cluster excitations. We first perform the variation after the angular-momentum and parity projections in the AMD framework (AMD+VAP) [105–107] to obtain the ground state wave function. Then we describe small amplitude motions by taking into account 1p-1h excitations on the obtained ground state wave function with the shifted basis AMD method as done in Ref. [108] for monopole excitations of ^{16}O. To take into account the large amplitude cluster motion, we combine the generator coordinate method (GCM) with the shifted basis AMD by superposing ^{5,6}He + α cluster wave functions. The angular-momentum and parity projections are performed in the present framework. Applying the present method, I investigate the dipole transitions ^{8}Be$(0^+_1) \to {}^{8}$Be(1^-), ^{9}Be$(3/2^-_1) \to {}^{9}$Be$(1/2^+,3/2^+,5/2^+)$, and ^{10}Be$(0^+_1) \to {}^{10}$Be(1^-).

This paper is organized as follows. The present method of AMD is formulated in Sec. II, and Sec. IV discusses the ground state structures and the $E1$ and isoscalar dipole (ISD) excitations in Be isotopes. The paper concludes with a summary in Sec. V.

II. FORMULATION OF AMD FOR DIPOLE EXCITATIONS

I apply the AMD+VAP method to obtain A-nucleon wave functions for the ground states of ^{8}Be, ^{9}Be, and ^{10}Be. To investigate dipole excitations, I use the shifted basis AMD to describe the 1p-1h excitation modes built on the ground state. I also perform the α-cluster GCM calculation combined with the shifted basis AMD to see how the α-cluster mode affects the dipole excitations. In this section, I explain the formulation of the AMD+VAP, the shifted basis AMD, and the α-cluster GCM calculations and also describe the definition of the dipole strengths.

A. AMD wave function

An AMD wave function is given by a Slater determinant,

$$\Phi_{\rm AMD}(\boldsymbol{Z}) = \frac{1}{\sqrt{A!}}\mathcal{A}\{\varphi_1,\varphi_2,\ldots,\varphi_A\}, \tag{1}$$

where $\mathcal{A}$ is the antisymmetrizer. The ith single-particle wave function φ_i is written by a product of spatial, spin, and isospin wave functions as

$$\varphi_i = \phi_{X_i}\chi_i\tau_i, \tag{2}$$

$$\phi_{X_i}(\boldsymbol{r}_j) = \left(\frac{2\nu}{\pi}\right)^{4/3}\exp\{-\nu(\boldsymbol{r}_j - \boldsymbol{X}_i)^2\}, \tag{3}$$

$$\chi_i = \left(\frac{1}{2}+\xi_i\right)\chi_\uparrow + \left(\frac{1}{2}-\xi_i\right)\chi_\downarrow, \tag{4}$$

where ϕ_{X_i} and χ_i are the spatial and spin functions, respectively, and τ_i is the isospin function fixed to be up (proton) or down (neutron). The width parameter ν is fixed to be the optimized value for each nucleus. To separate the center-of-mass motion from the total wave function $\Phi_{\rm AMD}(\boldsymbol{Z})$, the following condition should be satisfied:

$$\frac{1}{A}\sum_{i=1,\ldots,A}\boldsymbol{X}_i = 0. \tag{5}$$

In the present calculation, I keep this condition and exactly remove the contribution of the center-of-mass motion.

Accordingly, an AMD wave function is expressed by a set of variational parameters, $\boldsymbol{Z} \equiv \{\boldsymbol{X}_1,\ldots,\boldsymbol{X}_A,\xi_1,\ldots,\xi_A\}$, which specifies centroids of single-nucleon Gaussian wave packets and spin orientations for all nucleons. In the AMD framework, the existence of clusters is not assumed *a priori* because Gaussian centroids, $\boldsymbol{X}_1,\ldots,\boldsymbol{X}_A$, of all single-nucleon wave packets are independently treated as variational parameters. Nevertheless, a multicenter cluster wave function can be described by the AMD wave function with the corresponding configuration of Gaussian centroids. It should be noted that the AMD wave function is similar to the wave function used in fermionic molecular dynamics calculations [109,110].

B. AMD + VAP

In the AMD+VAP method, the parameters $\boldsymbol{Z} = \{\boldsymbol{X}_1,\boldsymbol{X}_2,\ldots,\boldsymbol{X}_A,\xi_1,\xi_2,\ldots,\xi_A\}$ in the AMD wave function are determined by the energy variation after the angular-momentum and parity projections (VAP). It means that $\boldsymbol{X}_i$ and ξ_i for the lowest J^π state are determined so as to minimize the energy expectation value of the Hamiltonian for the J^π-projected AMD wave function:

$$\frac{\delta}{\delta \boldsymbol{X}_i}\frac{\langle\Phi|H|\Phi\rangle}{\langle\Phi|\Phi\rangle} = 0, \tag{6}$$

$$\frac{\delta}{\delta \xi_i}\frac{\langle\Phi|H|\Phi\rangle}{\langle\Phi|\Phi\rangle} = 0, \tag{7}$$

$$\Phi = P^{J\pi}_{MK}\Phi_{\rm AMD}(\boldsymbol{Z}), \tag{8}$$

where $P^{J\pi}_{MK}$ is the angular-momentum and parity projection operator. After the VAP calculation, the optimized parameters $\boldsymbol{Z}^{J\pi}_{\rm VAP}$ for the lowest J^π state are obtained. For the ground state, the VAP with $J^\pi = 0^+$ and $K = 0$ is performed for ^{8}Be and ^{10}Be, and that with $J^\pi = 3/2^-$ and $K = 3/2$ is done for ^{9}Be. I denote the parameters $\boldsymbol{Z}^{J\pi}_{\rm VAP}$ obtained by the VAP for the ground state as $\boldsymbol{Z}^0 = \{\boldsymbol{X}^0_1,\ldots,\xi^0_1,\ldots\}$.

C. Shifted AMD

To take into account 1p-1h excitations, I consider the small variation of single-particle wave functions in the ground state wave function $\Phi_{\rm AMD}(\boldsymbol{Z}^0)$ by shifting the position of the Gaussian centroid of the ith single-particle wave function,

$\boldsymbol{X}_i^0 \to \boldsymbol{X}_i^0 + \epsilon \boldsymbol{e}_\sigma$, where ϵ is a small constant and $\boldsymbol{e}_\sigma$ is a unit vector with the label σ. In the present calculation, $\boldsymbol{e}_1, \ldots, \boldsymbol{e}_8$ for eight directions are adopted to obtain the approximately converged result for the $E1$ and ISD strengths. Details of the adopted unit vectors $\boldsymbol{e}_\sigma$ ($\sigma = 1, \ldots, 8$) are described in Sec. IV. For the spin part, I consider the spin-nonflip single-particle state χ_i and the spin-flip state $\bar{\chi}_i$ ($\langle \bar{\chi}_i | \chi_i \rangle = 0$),

$$\bar{\chi}_i = \left(\frac{1}{2} + \bar{\xi}_i\right)\chi_\uparrow + \left(\frac{1}{2} - \bar{\xi}_i\right)\chi_\downarrow, \tag{9}$$

where $\bar{\xi}_i = -1/4\xi_i^*$. For all single-particle wave functions, I consider spin-nonflip and spin-flip states shifted to eight directions independently and prepare $16A$ AMD wave functions, $\Phi_{\rm AMD}(\boldsymbol{Z}^0_{\rm nonflip}(i,\sigma))$ and $\Phi_{\rm AMD}(\boldsymbol{Z}^0_{\rm flip}(i,\sigma))$, with the shifted parameters

$$\begin{aligned}\boldsymbol{Z}^0_{\rm nonflip}(i,\sigma) \equiv \{&\boldsymbol{X}_1^{0\prime}, \ldots, \boldsymbol{X}_i^{0\prime} \\ &+ \epsilon\boldsymbol{e}_\sigma, \ldots, \boldsymbol{X}_A^{0\prime}, \xi_1^0, \ldots, \xi_i^0, \ldots, \xi_A^0\},\end{aligned} \tag{10}$$

$$\begin{aligned}\boldsymbol{Z}^0_{\rm flip}(i,\sigma) \equiv \{&\boldsymbol{X}_1^{0\prime}, \ldots, \boldsymbol{X}_i^{0\prime} \\ &+ \epsilon\boldsymbol{e}_\sigma, \ldots, \boldsymbol{X}_A^{0\prime}, \xi_1^0, \ldots, \bar{\xi}_i^0, \ldots, \xi_A^0\}.\end{aligned} \tag{11}$$

Here $\boldsymbol{X}_j^{0\prime}$ is chosen to be $\boldsymbol{X}_j^{0\prime} = \boldsymbol{X}_j^0 - \epsilon\boldsymbol{e}_\sigma/(A-1)$ to take into account the recoil effect so that the center-of-mass motion is separated exactly. Those shifted basis AMD wave functions $\Phi_{\rm AMD}(\boldsymbol{Z}^0_{\rm (non)flip}(i,\sigma))$ and the original wave function $\Phi_{\rm AMD}(\boldsymbol{Z}^0)$ are superposed to obtain the final wave functions for the ground and excited states,

$$\begin{aligned}&\Psi^{\rm sAMD}_{{\rm Be}(J_k^\pi)} \\ &= \sum_K c_0\left(J_k^\pi; K\right) P^{J\pi}_{MK} \Phi_{\rm AMD}(\boldsymbol{Z}^0) \\ &\quad + \sum_{i=1,\ldots,A}\sum_\sigma\sum_K c_1\left(J_k^\pi; i,\sigma,K\right) P^{J\pi}_{MK} \Phi_{\rm AMD}\left(\boldsymbol{Z}^0_{\rm nonflip}(i,\sigma)\right) \\ &\quad + \sum_{i=1,\ldots,A}\sum_\sigma\sum_K c_2\left(J_k^\pi; i,\sigma,K\right) P^{J\pi}_{MK} \Phi_{\rm AMD}\left(\boldsymbol{Z}^0_{\rm flip}(i,\sigma)\right),\end{aligned} \tag{12}$$

where the coefficients c_0, c_1, and c_2 are determined by diagonalization of the norm and Hamiltonian matrices. I call this method the "shifted basis AMD" (sAMD). The spin-nonflip version of the sAMD was applied to investigate monopole excitations of ^{16}O in Ref. [108].

I choose a small enough value of the spatial shift ϵ, typically $\epsilon = 0.1$ fm, so as to obtain ϵ-independent results. The model space of the sAMD contains the 1p-1h excitations that are written by a small shift of a single-nucleon Gaussian wave function of the ground state wave function. In the intrinsic frame before the angular-momentum and parity projections, the ground state AMD wave function is expressed by a Slater determinant, and, therefore, the sAMD method corresponds to the RPA in the restricted model space of the linear combination of shifted Gaussian wave functions. However, since the projected states are superposed in the sAMD, the coupling of the 1p-1h excitations with the rotation and parity transformation is properly taken into account. Therefore, the sAMD contains, in principle, higher correlations beyond the RPA in mean-field approximation.

It is clear from the Taylor expansion of a Gaussian that the shift $\boldsymbol{X}_i \to \boldsymbol{X}_i + \epsilon\boldsymbol{e}_\sigma$ of the Gaussian wave packet can be expressed by a linear combination of harmonic oscillator (HO) orbits around $\boldsymbol{X}_i$,

$$\phi_{\boldsymbol{X}_i + \epsilon\boldsymbol{e}_\sigma} \propto \sum_{k=0} \frac{1}{k!}(-2\epsilon)^k (\boldsymbol{r}\cdot\boldsymbol{e}_\sigma)^k \phi_{\boldsymbol{X}_i}. \tag{13}$$

In terms of the HO orbits around $\boldsymbol{X}_i$, the $O(\epsilon^0)$, $O(\epsilon^1)$, $O(\epsilon^2)$, and $O(\epsilon^3)$ terms cover $0s$, $\{0p\}$, $\{1s,0d\}$, and $\{1p,0f\}$ orbits, respectively. The $O(\epsilon)$ term contains $\boldsymbol{r}\phi_{\boldsymbol{X}_i}$ excited by the $E1$ operator, whereas the $O(\epsilon^3)$ term contains $r^2\boldsymbol{r}\phi_{\boldsymbol{X}_i}$ configurations excited by the ISD operator. Therefore, in the small ϵ limit, the number of independent vectors $\boldsymbol{e}_\sigma$ necessary to exactly cover the excited configurations $\boldsymbol{r}\phi_{\boldsymbol{X}_i}$ for $E1$ is three, and that $(r^2\boldsymbol{r}\phi_{\boldsymbol{X}_i})$ for ISD is $19 = 3 + 6 + 10$. Thus, the model space of the shifted Gaussian for each single-particle wave function is rather trivial; however, the model space of the sAMD is not trivial because of the recoil effect. Moreover, it is expected that, in the sAMD framework, the configurations excited by the $E1$ and ISD operators should be efficiently covered by a smaller number of $\boldsymbol{e}_\sigma$ because of the effects of the antisymmetrization and the angular-momentum and parity projections. To save the computational cost, I checked the convergence of the dipole strengths for the number of $\boldsymbol{e}_\sigma$ and chose a set of eight vectors as mentioned previously. Note that, when the recoil effect is omitted, the sAMD can be regarded as an extended AMD method, in which higher HO orbits are described as well as the default $0s$ orbit at $\boldsymbol{X}_i$ for the ith single-particle wave function. In the particular case of $\sigma = x, y, z$, it can be called the "p-wave AMD."

D. α-cluster GCM

In the ground state wave functions obtained by the AMD+VAP for ^{8}Be, ^{9}Be, and ^{10}Be, an α cluster is formed even though any clusters are not *a priori* assumed in the framework. Consequently, Gaussian centroids $\boldsymbol{X}_i^0$ for two protons and two neutrons are located at almost the same position. The intercluster motion of ^{5}He $+\,\alpha$ and ^{6}He $+\,\alpha$ structures in ^{9}Be and ^{10}Be can be excited by the dipole operators. To take into account the large amplitude α-cluster mode, we perform the α-cluster GCM (αGCM) calculation with respect to the intercluster distance. For simplicity, we label four nucleons composing the α cluster as $i = 1, \ldots, 4$ and other nucleons as $i = 5, \ldots, A$. The center-of-mass position of the α cluster is localized around $\boldsymbol{R}_\alpha = \frac{1}{4}{\rm Re}[\boldsymbol{X}_1^0 + \boldsymbol{X}_2^0 + \boldsymbol{X}_3^0 + \boldsymbol{X}_4^0]$. The intercluster distance D_α is written as

$$D_\alpha \equiv \left|{\rm Re}\left[\frac{1}{4}\sum_{i=1,\ldots,4}\boldsymbol{X}_i^0 - \frac{1}{A-4}\sum_{i=5,\ldots,A}\boldsymbol{X}_i^0\right]\right| = \frac{A}{A-4}R_\alpha \tag{14}$$

with $R_\alpha \equiv |\boldsymbol{R}_\alpha|$. To perform the αGCM calculation based on the ground state wave function $\Phi_{\rm AMD}(\boldsymbol{Z}^0)$, I changed the intercluster distance $D_\alpha \to D_\alpha + \Delta D$ by shifting positions of

single-nucleon Gaussian centroids $\boldsymbol{X}_i^0 \to \boldsymbol{X}_{i,D_\alpha}^0(\Delta D)$ by hand as

$$\boldsymbol{X}_{i,D_\alpha}^0(\Delta D) = \boldsymbol{X}_i^0 + \frac{A-4}{A}\Delta D\hat{\boldsymbol{R}}_\alpha \quad (i \leqslant 4), \tag{15}$$

$$\boldsymbol{X}_{i,D_\alpha}^0(\Delta D) = \boldsymbol{X}_i^0 - \frac{4}{A}\Delta D\hat{\boldsymbol{R}}_\alpha \quad (i > 4), \tag{16}$$

and superposing the wave functions with different ΔD values. I combined the αGCM with the sAMD and express the total wave function as

$$\begin{aligned}
&\Psi^{\text{sAMD}+\alpha\text{GCM}}_{\text{Be}(J_k^\pi)} \\
&= \sum_K c_0\left(J_k^\pi; K\right) P^{J\pi}_{MK}\Phi_{\text{AMD}}(\boldsymbol{Z}^0) \\
&\quad + \sum_{i=1,\ldots,A}\sum_\sigma\sum_K c_1\left(J_k^\pi; i,\sigma,K\right) P^{J\pi}_{MK}\Phi_{\text{AMD}}\left(\boldsymbol{Z}^0_{\text{nonflip}}(i,\sigma)\right) \\
&\quad + \sum_{i=1,\ldots,A}\sum_\sigma\sum_K c_2\left(J_k^\pi; i,\sigma,K\right) P^{J\pi}_{MK}\Phi_{\text{AMD}}\left(\boldsymbol{Z}^0_{\text{flip}}(i,\sigma)\right) \\
&\quad + \sum_{\Delta D}\sum_K c_3\left(J_k^\pi; \Delta D,K\right) P^{J\pi}_{MK}\Phi_{\text{AMD}}\left(\boldsymbol{Z}^0_{D_\alpha}(\Delta D)\right),
\end{aligned} \tag{17}$$

where $\boldsymbol{Z}^0_{D_\alpha}(\Delta D)\equiv\{\boldsymbol{X}^0_{1,D_\alpha}(\Delta D),\ldots,\boldsymbol{X}^0_{A,D_\alpha}(\Delta D),\xi_1,\ldots,\xi_A\}$. The coefficients are determined by diagonalization of the norm and Hamiltonian matrices.

III. ISOVECTOR AND ISOSCALAR DIPOLE TRANSITIONS

The $E1$ operator $\mathcal{M}(E1;\mu)$ is given by the isovector dipole operator as

$$\mathcal{M}(E1;\mu) = \frac{N}{A}\sum_i^{\text{proton}} r_i Y^1_\mu(\hat{\boldsymbol{r}}_i) - \frac{Z}{A}\sum_i^{\text{neutron}} r_i Y^1_\mu(\hat{\boldsymbol{r}}_i). \tag{18}$$

The ISD operator $\mathcal{M}(\text{IS1};\mu)$ is defined as

$$\mathcal{M}(\text{IS1};\mu) = \sum_i r_i^3 Y^1_\mu(\hat{\boldsymbol{r}}_i), \tag{19}$$

which excites the compressive dipole mode. The $E1$ and ISD strengths for the transition g.s. $\to J_k$ are given by the matrix elements of the dipole operators as

$$B(E1;\text{g.s.}\to J_k) = \frac{1}{2I_{\text{g.s.}}+1}|\langle J_k||\mathcal{M}(E1)||\text{g.s.}\rangle|^2, \tag{20}$$

$$B(\text{IS1};\text{g.s.}\to J_k) = \frac{1}{2I_{\text{g.s.}}+1}|\langle J_k||\mathcal{M}(\text{IS1})||\text{g.s.}\rangle|^2, \tag{21}$$

where $I_{\text{g.s.}}$ is the ground state angular momentum. The energy-weighted sum (EWS) of the $E1$ and ISD strengths is defined as

$$S(E1) \equiv \sum_{J_k} E_{J_k} B(E1;\text{g.s.}\to J_k), \tag{22}$$

$$S(\text{IS1}) \equiv \sum_{J_k} E_{J_k} B(\text{IS1};\text{g.s.}\to J_k), \tag{23}$$

where E_{J_k} is the energy of the J_k state. If the interaction commutes with the $E1$ operator, $S(E1)$ is identical to the TRK sum rule:

$$S(\text{TRK}) \equiv \frac{9\hbar^2}{8\pi m}\frac{NZ}{A}. \tag{24}$$

Since the nuclear interaction does not commute with the $E1$ operator, $S(E1)$ is usually enhanced from $S(\text{TRK})$.

In the present framework, all excited states are discrete states without escaping widths because the outgoing condition in the asymptotic region is not taken into account. I calculate the $E1$ and ISD strengths for discrete states and smear the strengths with a Gaussian by hand to obtain dipole strength functions as

$$\frac{dB(E1)}{dE} = \sum_J\sum_k \frac{\sqrt{\pi}}{\gamma} e^{-\frac{(E-E_{J_k})^2}{\gamma^2}} B(E1;\text{g.s.}\to J_k), \tag{25}$$

$$\frac{dB(\text{IS1})}{dE} = \sum_J\sum_k \frac{\sqrt{\pi}}{\gamma} e^{-\frac{(E-E_{J_k})^2}{\gamma^2}} B(\text{IS1};\text{g.s.}\to J_k), \tag{26}$$

where γ is the smearing width. The photonuclear cross section is dominated by $E1$ transitions and related to the $E1$ strength function as

$$\sigma(E) = \frac{16\pi^3}{9}\frac{e^2}{\hbar c}E\frac{dB(E1)}{dE}. \tag{27}$$

IV. RESULTS

A. Effective nuclear interactions

I used an effective nuclear interaction consisting of the central force of the MV1 force [111] and the spin-orbit force of the G3RS force [112,113] and the Coulomb force. The MV1 force is given by a two-range Gaussian two-body term and a zero-range three-body term. The G3RS spin-orbit force is a two-range Gaussian force. The Bartlett, Heisenberg, and Majorana parameters for case 1 of the MV1 force are $b = h = 0$ and $m = 0.62$, and the strengths of the G3RS spin-orbit force are $u_I = -u_{II} \equiv u_{ls} = 3000$ MeV. These interaction parameters are the same as those used in Refs. [105–107], in which the AMD+VAP calculation describes well the properties of the ground and excited states of ^{10}Be and ^{12}C.

B. Ground states

I performed the AMD+VAP calculation to obtain the ground state wave functions for $^8\text{Be}(0^+_1)$, $^9\text{Be}(3/2^-_1)$, and $^{10}\text{Be}(0^+_1)$. For comparison, I also applied it to $^4\text{He}(0^+_1)$. The width parameter was chosen to be $\nu = 0.20$ fm^{-2} for ^{8}Be and ^{9}Be, $\nu = 0.19$ fm^{-2} for ^{10}Be, and $\nu = 0.21$ fm^{-2} for ^{4}He to minimize the ground state energy. Figure 1(a) shows the intrinsic density distribution of the obtained wave functions $\Phi_{\text{AMD}}(\boldsymbol{Z}^0)$ for the ground states of Be. As seen in the density, the $\alpha+\alpha$, $^5\text{He}+\alpha$, and $^6\text{He}+\alpha$ cluster structures are developed in ^{8}Be, ^{9}Be, and ^{10}Be, respectively. Considering that the ^{5}He and ^{6}He clusters have $\alpha+n$ and $\alpha+2n$ structures, the ground states of ^{9}Be and ^{10}Be are regarded as the 2α cluster core with valence neutrons, $2\alpha+n$ and $2\alpha+2n$, in which the valence neutrons are localized around one of the 2α.

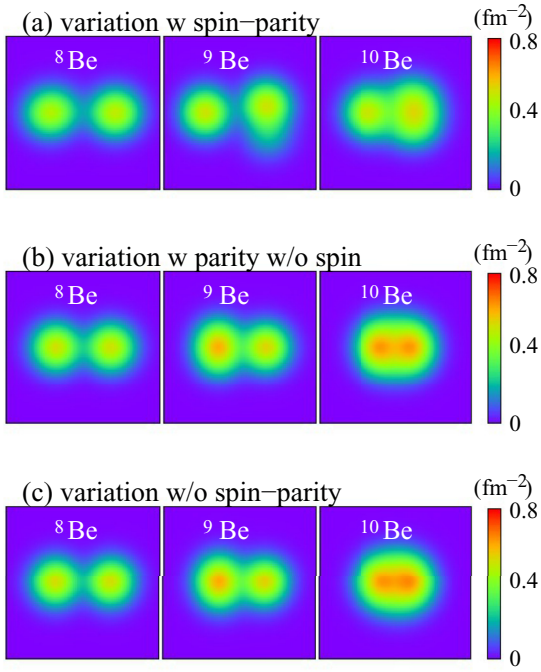

FIG. 1. Density distribution of the intrinsic wave functions of the ground states of ^{8}Be, ^{9}Be, and ^{10}Be obtained by (a) the AMD+VAP (variation after the angular-momentum and parity projections), (b) the variation after the parity projection without the angular-momentum projection, and (c) the variation without the angular-momentum and parity projections. The density integrated over the x axis is shown on the z-y plane in the $|z| \leqslant 5$ fm and $|y| \leqslant 5$ fm region.

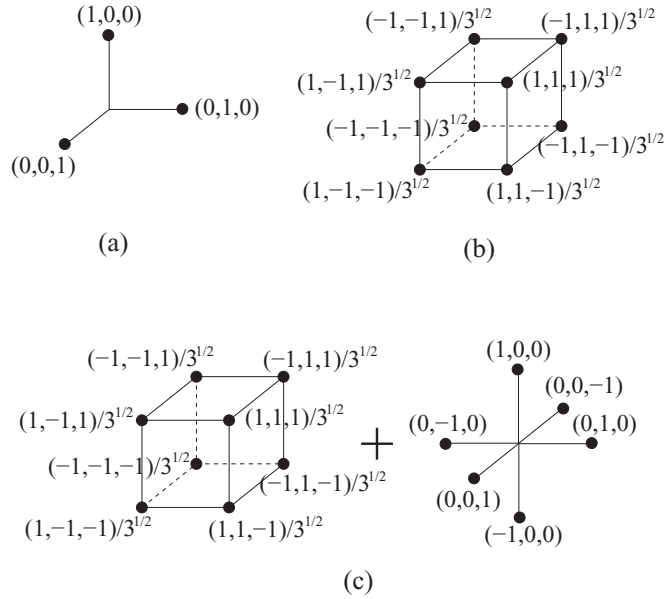

FIG. 2. Schematic figures for the sets of unit vectors (a) $\boldsymbol{e}_{\sigma=x,y,z}$, (b) $\boldsymbol{e}_{\sigma=1,\ldots,8}$, and (c) $\boldsymbol{e}_{\sigma=1,\ldots,14}$ used in the sAMD calculation.

As given in Eq. (1), an AMD wave function is expressed by a single Slater determinant. However, the projected state $P^{J\pi}_{MK}\Phi_{\rm AMD}(\boldsymbol{Z}^0)$ for the ground state wave function contains higher correlations beyond mean-field approximations, which is efficiently described by the VAP calculation. Indeed, cluster structures are remarkable in the present VAP result but they are relatively suppressed in calculations without the projections. For comparison with the present result obtained by the VAP (variation after the angular-momentum and parity projections), the result obtained by the variation without the angular-momentum and parity projections and that after the parity projection without the angular-momentum projection are also demonstrated in Figs. 1(b) and 1(c), respectively. It is clearly seen that the result of ^{10}Be obtained by the variation without the projections shows weak clustering with a parity-symmetric intrinsic structure [see the right-hand panels of Figs. 1(b) and 1(c)]. This indicates that the angular-momentum and parity projections in the energy variation are essential to obtain the parity-asymmetric structure with the ^{6}He $+\alpha$ correlation in ^{10}Be.

The root mean square radii of point-proton distribution of ^{8}Be, ^{9}Be, ^{10}Be, and ^{4}He calculated by the AMD+VAP are 2.73, 2.69, 2.43, and 1.64 fm, which are slightly larger than the experimental values, 2.39, 2.22, and 1.45 fm, of ^{9}Be, ^{10}Be, and ^{4}He reduced from the charge radii. The calculated magnetic and electric quadrupole moments of ^{9}Be are $\mu = -1.06\mu_N$ and $Q = 6.9\ e\ \text{fm}^2$, which reasonably agree to the experimental values, $\mu = -1.1778(9)\mu_N$ and $Q = 5.288(38)\ e\ \text{fm}^2$.

C. Excited states

To investigate dipole excitations, I calculated the $J^\pi = 1^-$ states of ^{8}Be, ^{10}Be, and ^{4}He, and $J^\pi = 1/2^+, 3/2^+$, and $5/2^+$ states of ^{9}Be by applying the sAMD based on the obtained ground state wave functions. The sAMD + αGCM is also applied to ^{9}Be and ^{10}Be. For the sAMD, the shift parameter ϵ is taken to be $\epsilon = 0.1$ fm, which is small enough to give the ϵ-independent result. For unit vectors $\boldsymbol{e}_\sigma$, I chose three sets, $\boldsymbol{e}_{\sigma=x,y,z}$, $\boldsymbol{e}_{\sigma=1,\ldots,8}$, and $\boldsymbol{e}_{\sigma=1,\ldots,14}$, as shown in Fig. 2, and checked the convergence of the dipole strengths. Here, the set of 8 vectors is $\boldsymbol{e}_{\sigma=1,\ldots,8} = (\pm 1/\sqrt{3}, \pm 1/\sqrt{3}, \pm 1/\sqrt{3})$, oriented to 8 corners of a cube, and that of 14 vectors is $\boldsymbol{e}_{\sigma=1,\ldots,14} = \{\boldsymbol{e}_{\sigma=1,\ldots,8}, \boldsymbol{e}_x, \boldsymbol{e}_y, \boldsymbol{e}_z, -\boldsymbol{e}_x, -\boldsymbol{e}_y, -\boldsymbol{e}_z\}$. The x, y, and z axes are taken to be the principle axes of the inertia of the intrinsic state that satisfy $\langle x^2\rangle \leqslant \langle y^2\rangle \leqslant \langle z^2\rangle$ and $\langle xy\rangle = \langle yz\rangle = \langle zx\rangle = 0$. The $E1$ and ISD strengths of ^{9}Be and ^{10}Be calculated by the sAMD in three cases, $\boldsymbol{e}_{\sigma=x,y,z}$, $\boldsymbol{e}_{\sigma=1,\ldots,8}$, and $\boldsymbol{e}_{\sigma=1,\ldots,14}$, are shown in Fig. 3. As expected, the set $\boldsymbol{e}_{\sigma=x,y,z}$ gives the approximately converged result for the $E1$ strength but not for the ISD strength. It is found that the set $\boldsymbol{e}_{\sigma=1,\ldots,8}$ is practically enough to get a qualitatively converged result for both the $E1$ and ISD strengths, and therefore this set is adopted in the present calculation of the dipole strengths. For the αGCM calculation, the distance parameter is taken to be $\Delta D = -1, 1, 2, \ldots, 20$ fm. In the ground state wave functions $\Phi_{\rm AMD}(\boldsymbol{Z}^0)$ of ^{9}Be (^{10}Be), the intercluster distance is $D_\alpha \sim 4$ fm (3 fm). Therefore, the choice of $\Delta D \leqslant 20$ fm means that α-cluster continuum states are treated as discretized states in the box boundary $D_\alpha \lesssim 24$ fm (23 fm).

The model space of the sAMD + αGCM wave function given in Eq. (17) covers 1p-1h excitations and α-cluster

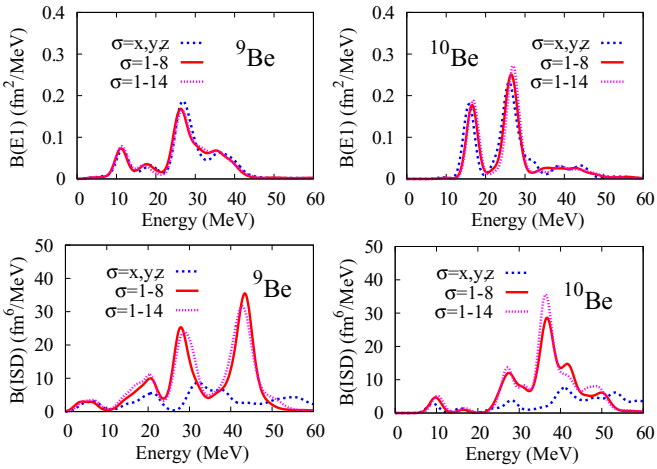

FIG. 3. $E1$ and ISD strengths of ^{9}Be and ^{10}Be obtained by the sAMD in the three cases $\boldsymbol{e}_{\sigma=x,y,z}$, $\boldsymbol{e}_{\sigma=1,\ldots,8}$, and $\boldsymbol{e}_{\sigma=1,\ldots,14}$. The smearing width is $\gamma = 2$ MeV.

excitations from the ground state wave function. For a detailed description of the low-lying energy spectra and their dipole transition strengths, I mixed additional configurations optimized for the low-lying levels $^9\mathrm{Be}(1/2^+_1)$, $^9\mathrm{Be}(3/2^+_1)$, $^9\mathrm{Be}(5/2^+_1)$, and $^{10}\mathrm{Be}(1^-_1)$, which are obtained by the AMD+VAP with $J^\pi = 1/2^+$, $3/2^+$, and $5/2^+$ for ^{9}Be and that with $J^\pi = 1^-$ for ^{10}Be. The final wave function with these additional VAP configurations (cfg) is given as

$$
\begin{aligned}
&\Psi^{\mathrm{sAMD}+\alpha\mathrm{GCM}+\mathrm{cfg}}_{\mathrm{Be}(J^\pi_k)} \\
&= \sum_K c_0\left(J^\pi_k; K\right) P^{J\pi}_{MK}\, \Phi_{\mathrm{AMD}}\left(\mathbf{Z}^0\right) \\
&\quad + \sum_{i=1,\ldots,A} \sum_\sigma \sum_K c_1\left(J^\pi_k; i,\sigma,K\right) P^{J\pi}_{MK}\, \Phi_{\mathrm{AMD}}\left(\mathbf{Z}^0_{\mathrm{nonflip}}(i,\sigma)\right) \\
&\quad + \sum_{i=1,\ldots,A} \sum_\sigma \sum_K c_2\left(J^\pi_k; i,\sigma,K\right) P^{J\pi}_{MK}\, \Phi_{\mathrm{AMD}}\left(\mathbf{Z}^0_{\mathrm{flip}}(i,\sigma)\right) \\
&\quad + \sum_{\Delta D} \sum_K c_3\left(J^\pi_k; \Delta D,K\right) P^{J\pi}_{MK}\, \Phi_{\mathrm{AMD}}\left(\mathbf{Z}^0_{D_\alpha}(\Delta D)\right) \\
&\quad + \sum_{J'\pi'} \sum_K c_4\left(J^\pi_k; J'\pi',K\right) P^{J\pi}_{MK}\, \Phi_{\mathrm{AMD}}\left(\mathbf{Z}^{J'\pi'}_{\mathrm{VAP}}\right). \qquad (28)
\end{aligned}
$$

The dipole strengths are calculated by the following matrix elements:

$$\left\langle \Psi^{\mathrm{sAMD}}_{\mathrm{Be}(J^\pi_k)} \middle|\middle| \mathcal{M} \middle|\middle| \Psi^{\mathrm{sAMD}}_{\mathrm{Be(g.s.)}} \right\rangle, \qquad (29)$$

$$\left\langle \Psi^{\mathrm{sAMD}+\alpha\mathrm{GCM}}_{\mathrm{Be}(J^\pi_k)} \middle|\middle| \mathcal{M} \middle|\middle| \Psi^{\mathrm{sAMD}+\alpha\mathrm{GCM}}_{\mathrm{Be(g.s.)}} \right\rangle, \qquad (30)$$

$$\left\langle \Psi^{\mathrm{sAMD}+\alpha\mathrm{GCM}+\mathrm{cfg}}_{\mathrm{Be}(J^\pi_k)} \middle|\middle| \mathcal{M} \middle|\middle| \Psi^{\mathrm{sAMD}+\alpha\mathrm{GCM}+\mathrm{cfg}}_{\mathrm{Be(g.s.)}} \right\rangle. \qquad (31)$$

The calculated dipole strengths with and without the additional VAP configurations are found to be almost consistent with each other except for quantitative details of the energy position and the strengths in $E \leqslant 10$ MeV. In this paper, I mainly discuss the dipole strengths calculated by the sAMD and the sAMD + αGCM + cfg wave functions, which I call cal-I and cal-II, respectively. The former corresponds to the small amplitude calculation containing 1p-1h excitations. The latter contains the large amplitude α-cluster mode in addition to the 1p-1h excitations described by the sAMD model space. Namely, the sAMD + αGCM + cfg includes the higher correlation than the sAMD in both the ground and excited states.

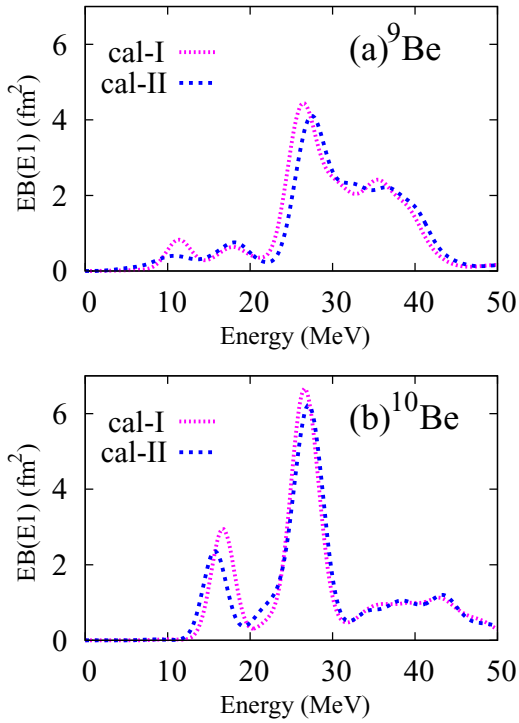

FIG. 4. Energy-weighted $E1$ strength of ^{9}Be and ^{10}Be obtained by the sAMD (cal-I) and the sAMD + αGCM + cfg (cal-II). The smearing width is $\gamma = 2$ MeV.

D. $E1$ strength

The energy-weighted $E1$ strength of ^{9}Be and ^{10}Be obtained by the sAMD (cal-I) and the sAMD + αGCM + cfg (cal-II) is shown in Fig. 4. The strength functions of two calculations (I) and (II) are qualitatively similar to each other except for broadening of the low-energy strength in $E \leqslant 15$ MeV of ^{9}Be in cal-II. Figure 5 shows the comparison of the calculated $E1$ cross section with the experimental photonuclear cross sections of ^{9}Be. In Table I, the EWS of the $E1$ strength in the low-energy ($E < 20$ MeV) and the GDR ($20 < E < 50$ MeV) regions and the total EWS in ^{9}Be and ^{10}Be obtained by the sAMD + αGCM + cfg (cal-II) are shown compared with the experimental values estimated by the experimental photonuclear cross sections [81,85]. The GDR energy calculated by the averaged energy in the $20 < E < 50$ MeV region, $E_{\mathrm{GDR}} = \int_{\mathrm{GDR}} E dB(E1) / \int_{\mathrm{GDR}} dB(E1)$, is also shown. The calculated total EWS of the $E1$ strength is enhanced from S(TRK) by a factor of 1.7. Compared with the experimental data for ^{9}Be, the calculation overestimates the EWS in the low-energy and GDR regions by a factor of 1.6 and underestimates the width of the GDR, whereas it reasonably describes the GDR energy and also the ratio of the EWS in the low-energy region to that of the GDR.

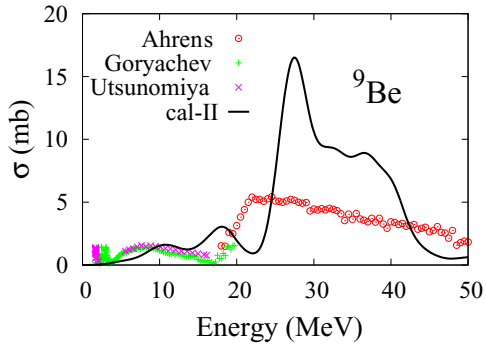

FIG. 5. Comparison of the calculated $E1$ cross section of ^{9}Be with the experimental photonuclear cross sections. The calculated values are those obtained with the sAMD + αGCM + cfg (cal-II), smeared by $\gamma = 2$ MeV. The experimental data are taken from the photonuclear cross sections by Ahrens *et al.* [85], the bremsstrahlung data by Goryachev *et al.* [81], and the photodisintegration cross sections by Utsunomiya *et al.* [84].

As shown in the comparison of the sAMD (cal-I) and the sAMD + αGCM + cfg (cal-II) in Fig. 4, the $E1$ strength of ^{9}Be and ^{10}Be is not affected so much by the coupling with the large amplitude α-cluster motion. In the following, I give a detailed analysis of the $E1$ strength of ^{8}Be, ^{9}Be, and ^{10}Be based on the sAMD to discuss the effects of excess neutrons on the $E1$ strength in ^{9}Be and ^{10}Be.

Figure 6 shows the $E1$ strength of ^{8}Be, ^{9}Be, ^{10}Be, and ^{4}He calculated by the sAMD. For ^{9}Be, decomposition of the transition strength to $J = 1/2^+$, $3/2^+$, and $5/2^+$ states is also shown. The GDR in ^{8}Be shows a two-peak structure in $E = 20$–40 MeV in contrast to the single-peak structure of the GDR in ^{4}He. Also in ^{9}Be, the two-peak structure of the GDR is seen but it somewhat broadens. In addition to the GDR, low-lying $E1$ strength appears in $E = 10$–20 MeV of ^{9}Be. In ^{10}Be, the lower peak of the GDR exists at $E \sim 25$ MeV, whereas the higher peak of the GDR is largely fragmented. Below the GDR, an $E1$ resonance appears at $E \sim 15$ MeV.

The origin of the two-peak structure of the GDR in Be isotopes is the prolate deformation of the 2α core. To distinguish the longitudinal mode in the intrinsic frame, we calculate the $E1$ strength in the truncated sAMD model space by using wave functions shifted only to the longitudinal (z)

TABLE I. EWS of the $E1$ strength in the low-energy ($E <$ 20 MeV) and the GDR ($20 < E < 50$ MeV) regions and the total EWS of ^{9}Be and ^{10}Be. The values in parentheses are the ratios to the TRK sum rule [$S(\mathrm{TRK}) = 33.0$ fm^2 MeV for ^{9}Be and $S(\mathrm{TRK}) = 35.6$ fm^2 MeV for ^{10}Be]. The calculated values are those obtained by the sAMD + αGCM + cfg (cal-II). The GDR energy is also shown. For ^{9}Be, the data evaluated from the experimental photonuclear cross sections [81,85] are listed. The unit of $S(E1)$ is fm^2 MeV.

	Expt.	cal-II	
	^{9}Be	^{9}Be	^{10}Be
$S(E1; E < 20)$	3.9 (0.12)	6.1 (0.19)	8.8 (0.25)
$S(E1; 20 < E < 50)$	29 (0.87)	46 (1.40)	47 (1.31)
$S(E1;$ total$)$		56 (1.70)	62 (1.74)
E_{GDR} (MeV)	30.9	31.4	29.6

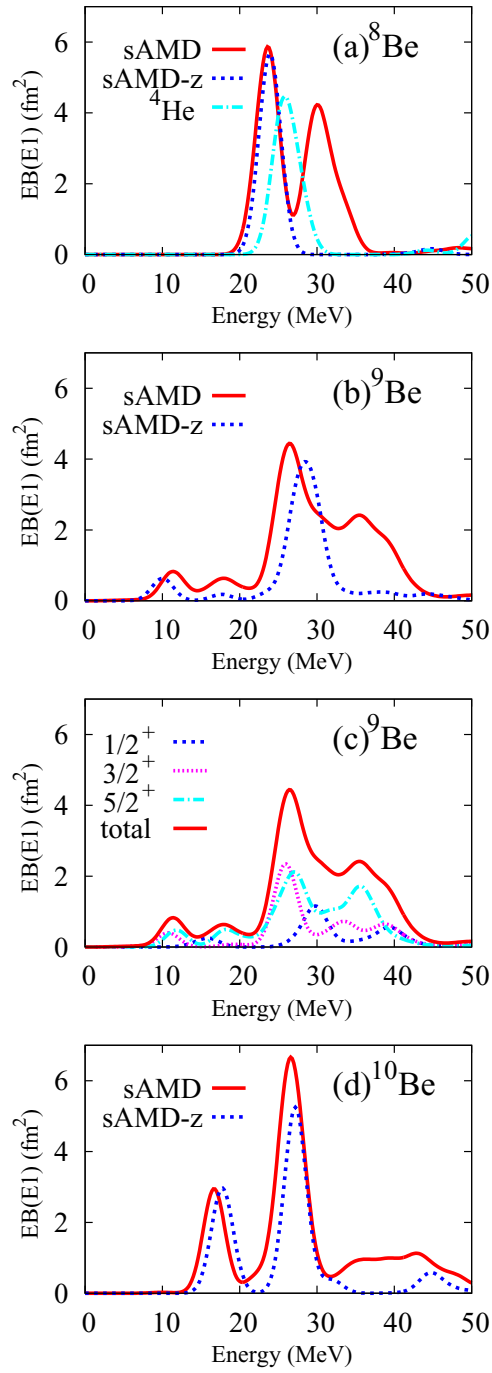

FIG. 6. Energy-weighted $E1$ strength of ^{8}Be, ^{9}Be, and ^{10}Be obtained by the sAMD ($\sigma = 1, \ldots, 8$) and the sAMD-z (longitudinal mode, $\sigma = z$) calculations. The sAMD and sAMD-z results for (a) ^{8}Be, (b) ^{9}Be, and (d) ^{10}Be are shown by solid and dashed lines, respectively. The decomposition of the strengths for $J^\pi = 1/2^+$, $3/2^+$, and $5/2^+$ states of ^{9}Be is also shown as well as the total strength in (c). For comparison, the energy-weighted $E1$ strength of ^{4}He obtained by the sAMD ($\sigma = 1, \ldots, 8$) is also shown in (a). The smearing width is $\gamma = 2$ MeV.

direction, that is, the sAMD with fixed $\sigma = z$ as

$$\Psi^{\text{sAMD-z}}_{\text{Be}(J^\pi_k)} = c_0\left(J^\pi_k\right) P^{J\pi}_{MK}\Phi_{\text{AMD}}(\mathbf{Z}^0) + \sum_{i=1,\ldots,A}\left\{c_1\left(J^\pi_k;i\right)P^{J\pi}_{M0}\Phi_{\text{AMD}}\left(\mathbf{Z}^0_{\text{nonflip}}(i,z)\right) + c_2\left(J^\pi_k;i\right)P^{J\pi}_{M0}\Phi_{\text{AMD}}\left(\mathbf{Z}^0_{\text{flip}}(i,z)\right)\right\}, \quad (32)$$

where the coefficients c_0, c_1, and c_2 are determined by diagonalization of the norm and Hamiltonian matrices. Here I omit the K-mixing and fix $K = 0$ for ^{8}Be and ^{10}Be, and $K = 3/2$ for ^{9}Be to take into account only the Y^1_0 mode in the intrinsic frame. The sAMD with $\sigma = z$, which I call "sAMD-z," is approximately regarded as the calculation containing the longitudinal mode but no transverse mode, though two modes do not exactly decouple from each other because of the angular-momentum projection. The $E1$ strength obtained by the sAMD-z is shown by dashed lines in Figs. 6(a), 6(b), and 6(d). In comparison of the sAMD and sAMD-z results, it is found that the lower peak of the GDR at $E = 20$–30 MeV is contributed by the longitudinal mode of the 2α core, whereas the higher peak of the GDR comes from the transverse mode. The higher peak broadens in ^{9}Be and it is largely fragmented in ^{10}Be, indicating that the transverse mode is affected by excess neutrons. For the low-lying $E1$ resonances below the GDR, the strength at $E \sim 10$ MeV in ^{9}Be and that at $E \sim 15$ MeV in ^{10}Be are mainly contributed by the longitudinal mode. These low-energy dipole resonances in ^{9}Be and ^{10}Be are understood by the longitudinal motion of valence neutrons against the 2α core.

From the above analysis of the $E1$ strength of ^{9}Be and ^{10}Be compared with that of ^{8}Be, the effects of excess neutrons on the $E1$ strength is understood as follows. The longitudinal and transverse dipole modes in the 2α core part contribute to the GDR with the two-peak structure. The valence neutron modes couple with the transverse dipole mode of the 2α core and they broaden the higher peak of the GDR. Moreover, the valence neutron modes against the 2α core contribute to the low-energy $E1$ strength. More details of the low-energy dipole excitations are discussed later.

E. ISD strength and coupling with the α-cluster mode in ^{9}Be and ^{10}Be

As previously mentioned, the sAMD (cal-I) corresponds to the small amplitude calculation, whereas the sAMD + αGCM + cfg (cal-II) contains the large amplitude α-cluster mode. A possible enhancement of the ISD strength in cal-II relative to cal-I can be a good probe for the dipole excitation that couples with the α-cluster mode, because the α-cluster excitation in ^{9}Be and ^{10}Be involves the compressive dipole mode. The energy-weighted ISD strength of ^{9}Be and ^{10}Be calculated by cal-I and cal-II is shown in Fig. 7. The strength of the isoscalar GDR in $E = 30 \sim 50$ MeV is not affected by the α-cluster mode, whereas the ISD strength for some low-energy resonances are significantly enhanced in cal-II as a result of the coupling with the α-cluster mode. In ^{9}Be, the ISD strength in $E < 10$ MeV is remarkably enhanced in cal-II, whereas the resonance at $E = 10$–15 MeV has the weak ISD strength in both cal-I and cal-II. In ^{10}Be, the ISD strength around $E = 15$ MeV is enhanced.

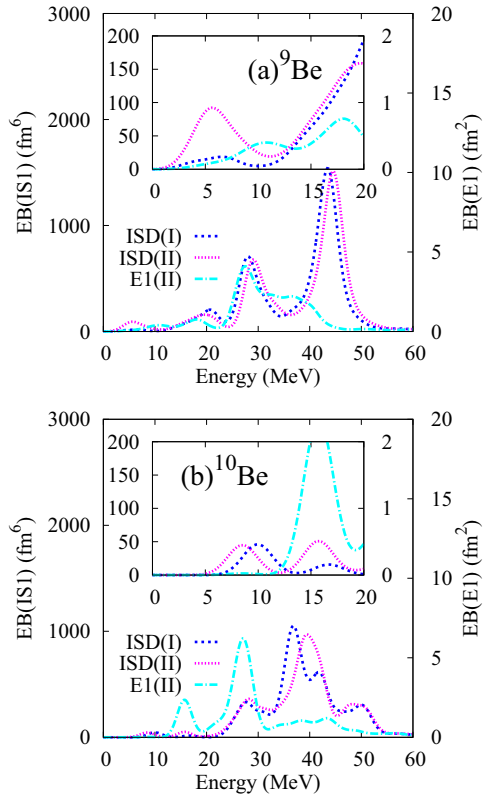

FIG. 7. ISD strength of ^{9}Be and ^{10}Be obtained by the sAMD (cal-I) and the sAMD + αGCM + cfg (cal-II). $E1$ strength obtained by the the sAMD + αGCM + cfg (cal-II) is also shown for comparison. The smearing width is $\gamma = 2$ MeV.

F. Low-energy dipole resonances in ^{9}Be and ^{10}Be

From the analysis of the $E1$ and ISD strengths, the low-energy dipole excitations below the GDR in ^{9}Be can be categorized as three resonances in $E < 8$ MeV, $8 < E < 15$ MeV, and $15 < E < 20$ MeV, which I label A1, A2, and A3 resonances, respectively. The A1 resonance contains the contribution from the low-lying positive-parity states, ^{9}Be$(1/2^+_1)$, ^{9}Be$(3/2^+_1)$, and ^{9}Be$(5/2^+_1)$, which are discussed in detail later. The EWS in the corresponding energy regions, $S(E1/\text{IS1};\text{A1})$, $S(E1/\text{IS1};\text{A2})$, and $S(E1/\text{IS1};\text{A3})$, is listed in Table II as well as the total EWS value. In addition to the EWS obtained by the sAMD (cal-I) and sAMD + αGCM + cfg (cal-II), the EWS calculated by the matrix elements

$$\left\langle \Psi^{\text{sAMD}}_{\text{Be}(J^\pi_k)} \middle| \mathcal{M} \middle| \Psi^{\text{sAMD}+\alpha\text{GCM}+\text{cfg}}_{\text{Be(g.s.)}} \right\rangle \quad (33)$$

for the transitions from the sAMD + αGCM + cfg initial states to the sAMD final states (cal-III) and that by the matrix elements

$$\left\langle \Psi^{\text{sAMD}+\alpha\text{GCM}+\text{cfg}}_{\text{Be}(J^\pi_k)} \middle| \mathcal{M} \middle| \Psi^{\text{sAMD}}_{\text{Be(g.s.)}} \right\rangle \quad (34)$$

for the transitions from the sAMD initial states to the sAMD + αGCM + cfg final states (cal-IV) are also shown

TABLE II. EWS of the $E1$ and ISD strengths for low-energy resonances: A1 ($E < 8$ MeV), A2 ($8 < E < 15$ MeV), and A3 ($15 < E < 20$ MeV) in ^{9}Be, and B1 ($E < 12$ MeV) and B2 ($12 < E < 20$ MeV) in ^{10}Be. The total EWS is also shown. The strengths are calculated by the sAMD (cal-I) and the sAMD + αGCM + cfg (cal-II). The EWS calculated by the matrix elements for the transitions from the sAMD + αGCM + cfg initial states to the sAMD final states (cal-III), and that for the transitions from the sAMD initial states to the sAMD + αGCM + cfg final states (cal-IV) are also listed. The unit of $S(E1)$ is fm^2 MeV and that of S(ISD) is fm^6 MeV.

	I	II	III	IV
α mode in initial	without	with	with	without
α mode in final	without	with	without	with
		^{9}Be		
$S(E1;\text{total})$	58	56	58	56
$S(E1;\text{A1})$	0.13	0.43	0.39	0.16
$S(E1;\text{A2})$	3.3	2.4	2.6	3.5
$S(E1;\text{A3})$	2.7	3.3	3.3	2.6
$S(\text{IS1};\text{total})$	15.2×10^3	15.3×10^3	15.2×10^3	15.3×10^3
$S(\text{IS1};\text{A1})$	93	410	58	124
$S(\text{IS1};\text{A2})$	108	230	200	131
$S(\text{IS1},\text{A3})$	490	560	640	520
		^{10}Be		
$S(E1;\text{total})$	63	62	63	62
$S(E1;\text{B1})$	0.09	0.08	0.06	0.10
$S(E1;\text{B2})$	10.4	8.7	7.6	10.9
$S(\text{IS1};\text{total})$	12.7×10^3	13.0×10^3	12.7×10^3	13.0×10^3
$S(\text{IS1};\text{B1})$	162	157	115	187
$S(\text{IS1};\text{B2})$	56	187	83	74

in the table. Here cal-III contains the α-cluster mode in the initial states as the ground state correlation but not in the final states, whereas cal-IV contains the α-cluster mode only in the final states but not in the initial states. In all the calculations (cal-I, cal-II, cal-III, and cal-IV), $S(E1;\text{A1})$ is very small, whereas $S(E1;\text{A2})$ and $S(E1;\text{A3})$ are significantly large as $\sim$10% of the TRK sum rule. Consequently, the EWS of the $E1$ strength in $E < 20$ MeV exhausts $\sim$20% of the TRK sum rule and it is $\sim$10% of the calculated total EWS.

The α-cluster mode does not affect so much the $E1$ and ISD strengths of A2 and those of A3, but it gives significant enhancement of the dipole strengths of A1. In particular, $S(\text{IS1};\text{A1})$ is remarkably enhanced by the coupling with the α-cluster mode. The enhancement is found only in cal-II but not in other calculations (cal-I, cal-III, and cal-IV). It indicates that the coupling with the α-cluster mode in the ground state and that in the A1 resonance coherently enhance $S(\text{IS1};\text{A1})$. The α-cluster mode also makes $S(E1;\text{A1})$ three times larger in cal-II than in cal-I, though it is still less than 2% of the TRK sum rule.

As seen in the EWS of the sAMD + αGCM + cfg (cal-II) in Table II, the A1 resonance shows relatively strong ISD and weak $E1$ transitions, whereas the A2 resonance shows relatively weak ISD and strong $E1$ transitions. In the sAMD + αGCM + cfg, the wave functions for these resonances are expressed by the linear combination of many configurations; however, each of the low-lying resonances has

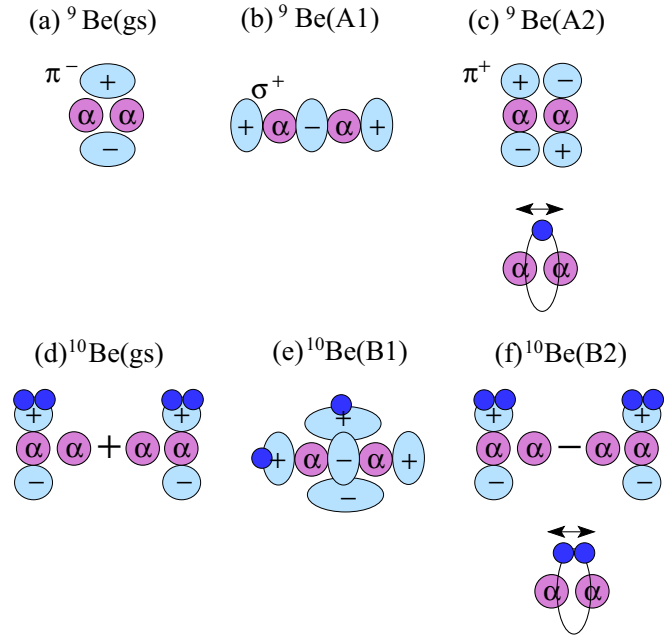

FIG. 8. Schematic figures of 2α and valence neutrons for the ground state and the A1 and A2 resonances of ^{9}Be, and those for the ground state and the B1 and B2 resonances of ^{10}Be.

a dominant component given by the single J^π-projected AMD wave function obtained by the AMD + VAP. Based on the analysis of the single-particle wave functions in the dominant component, the above-mentioned characteristics of the A1 and A2 resonances can be understood by the molecular orbital $2\alpha + n$ picture as follows.

The ground and low-lying states of ^{9}Be are approximately described by the molecular orbital structure, where the valence neutron occupies molecular orbitals formed by the linear combination of p orbits around α clusters as already discussed in Refs. [86,87,114,115]. Let me consider two α clusters at the left and right along the z axis (see Fig. 8). I call the left (right) α "$\alpha_{L(R)}$," and label single-particle orbits (atomic orbitals) around each α cluster as $[Nn_zl_zj_z]_{\alpha_{L(R)}}$. Here N is the total quantum (node) number, n_z is the quantum number for the z axis, and l_z and j_z are the z components of the orbital and total-angular momenta, respectively. The $\pi^-_{3/2}$ and $\pi^+_{3/2}$ molecular orbitals are given by the linear combination of the atomic orbitals $[101\frac{3}{2}]_{\alpha_{L,R}}$ as

$$\pi^-_{3/2} \equiv \left[101\frac{3}{2}\right]_{\text{MO}} = \left[101\frac{3}{2}\right]_{\alpha_L} + \left[101\frac{3}{2}\right]_{\alpha_R}, \quad (35)$$

$$\pi^+_{3/2} \equiv \left[211\frac{3}{2}\right]_{\text{MO}} = \left[101\frac{3}{2}\right]_{\alpha_L} - \left[101\frac{3}{2}\right]_{\alpha_R}, \quad (36)$$

where $[Nn_zl_zj_z]_{\text{MO}}$ is the label indicating the quantum numbers N, n_z, l_z, and j_z of the molecular orbital around the 2α. Another molecular orbital is the longitudinal orbital $\sigma^+_{1/2}$ given by the linear combination of $[110\frac{1}{2}]_{\alpha_{L,R}}$ as

$$\sigma^+_{1/2} \equiv \left[220\frac{3}{2}\right]_{\text{MO}} = \left[110\frac{1}{2}\right]_{\alpha_L} - \left[110\frac{1}{2}\right]_{\alpha_R}. \quad (37)$$

In the case that the α-α distance is not so large, the molecular orbital $[Nn_z l_z j_z]_{\rm MO}$ approximately corresponds to the Nilsson (deformed shell-model) orbit $[Nn_3\Lambda]_\Omega$ with $n_3 = n_z$, $\Lambda = l_z$, and $\Omega = j_z$ in the prolate deformation. $\pi^-_{3/2}$ is the negative-parity orbital with no node ($n_z = 0$), $\pi^+_{3/2}$ is the positive-parity orbital with one node ($n_z = 1$), and $\sigma^+_{1/2}$ is the positive-parity orbital with two nodes ($n_z = 2$) along the z axis. For the valence neutron around the 2α, $\pi^-_{3/2}$ is the lowest negative-parity molecular orbital, whereas $\sigma^+_{1/2}$ is the lowest positive-parity orbital.

The ground state of ^{9}Be dominantly has the $2\alpha + n$ structure with the $\pi^-_{3/2}$ configuration. The A1 resonance is approximately described by the $\sigma^+_{1/2}$ configuration, whereas the A2 resonance is dominated by the $\pi^+_{3/2}$ configuration (see Fig. 8). The $E1$ transition for $\pi^-_{3/2} \to \pi^+_{3/2}$, i.e., $[101\frac{3}{2}]_{\rm MO} \to [211\frac{3}{2}]_{\rm MO}$, is possible because the Y^1_0 operator changes $N \to N \pm 1$ and $n_z \to n_z \pm 1$. However, the $E1$ transition for $\pi^-_{3/2} \to \sigma^+_{1/2}$, i.e., $[101\frac{3}{2}]_{\rm MO} \to [220\frac{1}{2}]_{\rm MO}$, is forbidden because the change $n_z \to n_z \pm 2$ is not possible for the $E1$ operator. This is the reason why the $E1$ strength is large for A2 but it is suppressed for A1. Because of the $[211\frac{3}{2}]_{\rm MO}$ configuration of the A2 resonance, the $E1$ strength of A2 shows the $K = 3/2$ band feature that the contribution from transitions to $J^\pi = 3/2^+$ and $5/2^+$ states is dominant as seen in Fig. 6(c). The A1 resonance has the larger node number $n_z = 2$ along the 2α direction than the A2 resonance ($n_z = 1$) and, therefore, the spatial development of the 2α clustering is more prominent in the A1 resonance. As a result of the developed clustering, the A1 resonance couples rather strongly with the α-cluster mode. The coupling with the α-cluster mode, namely, the ^{5}He-α relative motion in A1, enhances the ISD strength as discussed previously.

In Fig. 9, I show the single-particle wave function of the valence neutron around the 2α core in the dominant components of the ground state, A1, and A2 resonances. The analysis of the single-particle wave functions is similar to that done in Ref. [106] for ^{10}Be. The dominant components of the ground state and the A1 resonance of ^{9}Be are $P^{J\pi}_{MK}\Phi_{\rm AMD}(\boldsymbol{Z}^{J\pi}_{\rm VAP})$ obtained by the VAP for $J^\pi = 3/2^-$ and $J^\pi = \{1/2^+, 3/2^+, 5/2^+\}$, respectively. The A2 resonance is dominated by the $3/2^+$ and $5/2^+$ components projected from $\Phi_{\rm AMD}(\boldsymbol{Z}^{3/2-}_{\rm VAP} = \boldsymbol{Z}^0)$ obtained by the VAP for the ground state. It is found that the negative-parity and positive-parity components of the valence neutron in $\Phi_{\rm AMD}(\boldsymbol{Z}^0)$ approximately correspond to the molecular $\pi^-_{3/2}$ and $\pi^+_{3/2}$ orbitals [see Figs. 8(a) and 8(c)], respectively, and the positive-parity component of the valence neutron in $\Phi_{\rm AMD}(\boldsymbol{Z}^{J\pi}_{\rm VAP})$ for $J^\pi = 1/2^+$, $J^\pi = 3/2^+$, and $J^\pi = 5/2^+$ shows the two-node structure corresponding approximately to the molecular $\sigma^+_{1/2}$ orbital [see Fig. 8(b)]. These results support the above-mentioned interpretation of the ground state, A1, and A2 resonances with the molecular $\pi^-_{3/2}$, $\sigma^+_{1/2}$, and $\pi^+_{3/2}$ orbitals, respectively.

Let me discuss low-energy dipole resonances in ^{10}Be. The low-energy dipole strength below the GDR can be categorized as two resonances in $E < 12$ MeV and $12 < E < 20$ MeV, which I label B1 and B2, respectively. The EWS of the dipole strengths for the corresponding energy regions are

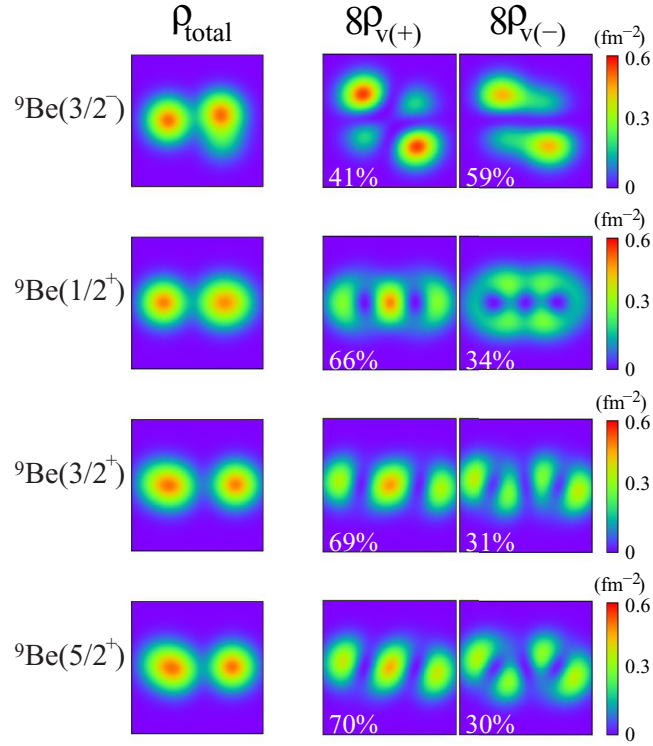

FIG. 9. Valence neutron wave functions in the intrinsic wave functions, $\Phi_{\rm AMD}(\boldsymbol{Z}^{J\pi}_{\rm VAP})$, of ^{9}Be obtained by the VAP for $J^\pi = 3/2^-$ and $J^\pi = \{1/2^+, 3/2^+, 5/2^+\}$. The distribution of the total density is shown on the left. The density distributions of the positive- and negative-parity components of the valence neutron wave function are shown in the middle and on the right. The total density is normalized to be the nucleon number A, whereas each of the positive- and negative-parity components is normalized to be 1 and the factor 8 is multiplied in the illustration. The percentages of the positive and negative components are also shown. The density integrated over the x axis is shown on the z-y plane in the $|z| \leqslant 5$ fm and $|y| \leqslant 5$ fm region.

listed in Table II. The B2 resonance shows the strong $E1$ transition exhausting more than 20% of the TRK sum rule and 10% of the calculated total EWS. It also shows the significant ISD strength enhanced by the α-cluster mode in cal-II (sAMD + αGCM + cfg). The significant $E1$ strength and the strong coupling with the α-cluster mode of the B2 resonance can be understood by two-neutron correlation in the $2\alpha + 2n$ picture as shown in the schematic figures of Fig. 8. The configuration in the ground state of ^{10}Be is approximately described by the positive-parity projected state of the atomic orbital configuration as

$$\left[101\frac{3}{2}\right]_{\alpha_L}\left[10-1-\frac{3}{2}\right]_{\alpha_L} + \left[101\frac{3}{2}\right]_{\alpha_R}\left[10-1-\frac{3}{2}\right]_{\alpha_R} = \frac{1}{2}\left\{\left(\pi^-_{3/2}\right)^2 + \left(\pi^+_{3/2}\right)^2\right\}, \quad (38)$$

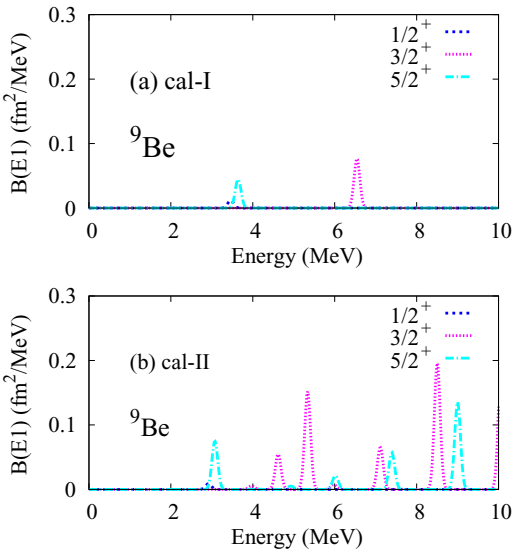

FIG. 10. $E1$ strength of $1/2^+$, $3/2^+$, and $5/2^+$ states of ^{9}Be in $E < 10$ MeV obtained by (a) sAMD (cal-I) and (b) sAMD + αGCM + cfg (cal-II). The smearing width is $\gamma = 0.1$ MeV.

which corresponds to the ^{6}He + α cluster structure in the intrinsic state of the ^{10}Be ground state. The B2 resonance has 50% overlap with the negative-parity state $P^{1-}_{00}\Phi_{\rm AMD}(\mathbf{Z}^0)$ projected from the intrinsic wave function for the ground state and, hence, the B2 resonance is interpreted as the parity partner of the ground state as

$$\left[101\frac{3}{2}\right]_{\alpha_L}\left[10-1-\frac{3}{2}\right]_{\alpha_L}-\left[101\frac{3}{2}\right]_{\alpha_R}\left[10-1-\frac{3}{2}\right]_{\alpha_R}$$
$$=\frac{1}{2}\left\{\pi^-_{3/2}\pi^+_{3/2}+\pi^+_{3/2}\pi^-_{3/2}\right\}. \quad (39)$$

In the transition from the ground state to the B2 resonance, the coherent contribution of two neutrons enhances the $E1$ strength. The B2 resonance has also a large overlap with negative-parity ^{6}He + α cluster wave functions, for instance, 60% overlap with $P^{1-}_{00}\Phi_{\rm AMD}(\mathbf{Z}^0_{D_\alpha}(\Delta D = 1\,\text{fm}))$. As a result of the strong coupling with the α-cluster mode, the ISD strength of the B2 resonance is enhanced. In other words, the B2 resonance is regarded as the α-cluster excitation on the ground state which already contains the ^{6}He + α cluster structure. In contrast to the B2 resonance, the B1 resonance is regarded as a single-particle excitation with the molecular orbital configuration $\pi^-_{3/2}\sigma^+_{1/2}$ from the analysis of the single-particle wave functions as discussed for ^{10}Be(1^-_1) in Ref. [106]. This configuration has no coherent contribution of two neutrons to the $E1$ strength. Moreover, the $\pi^-_{3/2}\sigma^+_{1/2}$ configuration contains the ^{5}He + ^{5}He and ^{6}He* + α components instead of the ^{6}He + α component and, therefore, it does not couple with the α-cluster mode.

Finally, I discuss the calculated $B(E1)$ of the $1/2^+_1$, $3/2^+_1$, and $5/2^+_1$ states of ^{9}Be, which contribute to the dipole strengths of the A1 resonance. In Fig. 10, I show the $E1$ strength in $E \leqslant 10$ MeV of ^{9}Be. Here the smearing width is chosen to be $\gamma = 0.1$ MeV to resolve discrete states. The $1/2^+_1$, $3/2^+_1$, and $5/2^+_1$ states are obtained as discrete states in the sAMD (cal-I). In the sAMD + αGCM + cfg (cal-II), the $1/2^+_1$ and $5/2^+_1$ states are still discrete states; however, the $3/2^+_1$ state shows a resonance behavior coupling with the discretized continuum states in the box boundary at $D_\alpha \lesssim 24$ fm. We evaluate $B(E1)$ of the $3/2^+_1$ resonance by a sum of the $E1$ strength in $E < 6$ MeV and estimate the excitation energy by the $B(E1)$ weighted-averaged energy of $3/2^+$ states in this energy region. In Table III, I compare the calculated $E1$ strength of the $1/2^+_1$, $3/2^+_1$, and $5/2^+_1$ states with the experimental values measured by the (γ,n) cross sections in Ref. [83]. The excitation energies and $B(E1)$ of ^{9}Be($5/2^+_1$) and ^{9}Be($3/2^+_1$) obtained by the sAMD + αGCM + cfg (cal-II) reproduce reasonably the experimental data, whereas the calculated $B(E1)$ of ^{9}Be($1/2^+_1$) is quite small, inconsistently with the experimental data. The $1/2^+_1$ state has been suggested to be a virtual or resonance state of an s-wave neutron [91–97]. However, the present model is insufficient to describe such a virtual or s-wave resonance state because of the valence neutron motion far from the 2α. It means that neutron decay is not taken into account in the model space even though the calculated one-neutron separation energy ($S_n = 0.5$ MeV in the AMD + VAP and $S_n = 2.1$ MeV in the sAMD) is not so much different from the experimental value ($S_n = 1.67$ MeV). In the present calculation, ^{9}Be($1/2^+_1$), ^{9}Be($3/2^+_1$), and ^{9}Be($5/2^+_1$) dominantly have the $2\alpha + n$ structure with a valence neutron in the $\sigma^+_{1/2}$ orbital as described previously. Since the intrinsic structures of the dominant components of these three states are similar to each other as shown in Fig. 9, they are approximately regarded as the band members of the $K^\pi = 1/2^+$ rotational band. It should be commented that only ^{9}Be($3/2^+_1$) and ^{9}Be($5/2^+_1$) contribute to the ISD strength of the A1 resonance because of the coupling with the cluster mode, but ^{9}Be($1/2^+_1$) gives almost no contribution to the dipole strengths in the present result.

TABLE III. Excitation energy and $E1$ strength of ^{9}Be($1/2^+_1$), ^{9}Be($3/2^+_1$), ^{9}Be($5/2^+_1$), and ^{10}Be(1^-_1). The energy (MeV) and $B(E1)$ (fm^2) calculated by the sAMD (cal-I) and the sAMD + αGCM + cgf (cal-II) are listed compared with the experimental data. The experimental values of ^{9}Be are data measured by the (γ,n) cross sections in Ref. [83]. The experimental excitation energy of ^{10}Be(1^-) is taken from Refs. [116,117].

	cal-I		cal-II		Expt.	
	E	$B(E1)$	E	$B(E1)$	E	$B(E1)$
^{9}Be						
$1/2^+$	3.5	0.002	2.9	0.002	1.731(2)	0.136(2)
$3/2^+$	6.5	0.014	5.1	0.039	4.704	0.068(7)
$5/2^+$	3.6	0.008	3.1	0.013	3.008(4)	0.016(2)
^{10}Be						
1^-	9.8	0.009	8.3	0.010	5.960	

V. SUMMARY

I investigated the isovector and isoscalar dipole excitations in ^{9}Be and ^{10}Be with the shifted basis AMD combined with the α-cluster GCM, in which the 1p-1h excitation modes built

on the ground state and the large amplitude α-cluster mode are taken into account. Since the angular-momentum and parity projections are done, the coupling of excitations in the intrinsic frame with the rotation and parity transformation is taken into account microscopically. The low-energy $E1$ resonances appear in $E < 20$ MeV because of valence neutron modes against the 2α core. They exhaust about 20% of the TRK sum rule and 10% of the calculated EWS. The GDR shows the two-peak structure which is understood by the $E1$ excitations in the 2α core part with the prolate deformation. The higher peak of the GDR for the transverse mode broadens in ^{9}Be and it is largely fragmented in ^{10}Be because of excess neutrons.

By comparing the results of the shifted basis AMD combined with and without the α-cluster GCM, I investigated how the $E1$ and ISD strengths in ^{9}Be and ^{10}Be are affected by the large amplitude α-cluster mode. The ISD strength is a good probe to identify the dipole resonances that couple with the α-cluster mode because the α-cluster mode in ^{9}Be and ^{10}Be involves the compressive dipole mode. It was found that the ISD strengths for some low-energy resonances in ^{9}Be and ^{10}Be are enhanced by the coupling with the α-cluster mode, whereas the $E1$ strength is not so sensitive to the coupling with the α-cluster mode. In ^{9}Be, the ISD strength of the low-energy resonance in $E < 10$ MeV is remarkable. In ^{10}Be, the ISD strength at $E \sim 15$ MeV is enhanced by the coupling with the α-cluster mode. This resonance at $E \sim 15$ MeV in ^{10}Be is regarded as the α-cluster excitation on the ground state having the ^{6}He $+\alpha$ structure and can be interpreted as the parity partner of the ground state. The $E1$ transition of this resonance is also strong because of the coherent contribution of two valence neutrons.

Compared with the experimental $E1$ strength of ^{9}Be estimated by the photonuclear cross sections, the calculation overestimates the EWS in the low-energy ($E < 20$ MeV) and GDR ($20 < E < 50$ MeV) regions by a factor of 1.6 and underestimates the width of the GDR, whereas it reasonably describes the GDR energy and also the ratio of the EWS in the low-energy region to that of the GDR. For the low-lying positive-parity states of ^{9}Be, the calculated excitation energies and $B(E1)$ of ^{9}Be($5/2^{+}_{1}$) and ^{9}Be($3/2^{+}_{1}$) reasonably agree with the experimental data. However, the calculation fails to reproduce the experimental $B(E1)$ of ^{9}Be($1/2^{+}_{1}$) because the present model is insufficient to describe the detailed asymptotic behavior of the s-wave neutron in the $1/2^{+}_{1}$ state.

ACKNOWLEDGMENTS

The author would like to thank Dr. Utsunomiya and Dr. Kikuchi for fruitful discussions. The computational calculations of this work were performed by using the supercomputer in the Yukawa Institute for theoretical physics, Kyoto University. This work was supported by JSPS KAKENHI Grant No. 26400270.

[1] T. Kobayashi *et al.*, Phys. Lett. B **232**, 51 (1989).
[2] K. Ieki *et al.*, Phys. Rev. Lett. **70**, 730 (1993).
[3] D. Sackett *et al.*, Phys. Rev. C **48**, 118 (1993).
[4] S. Shimoura *et al.*, Phys. Lett. B **348**, 29 (1995).
[5] M. Zinser *et al.*, Nucl. Phys. A **619**, 151 (1997).
[6] T. Aumann *et al.*, Phys. Rev. C **59**, 1252 (1999).
[7] T. Nakamura *et al.*, Phys. Rev. Lett. **96**, 252502 (2006).
[8] R. Kanungo *et al.*, Phys. Rev. Lett. **114**, 192502 (2015).
[9] D. J. Millener, J. W. Olness, E. K. Warburton, and S. S. Hanna, Phys. Rev. C **28**, 497 (1983).
[10] R. Palit *et al.*, Phys. Rev. C **68**, 034318 (2003).
[11] T. Nakamura *et al.*, Phys. Lett. B **394**, 11 (1997).
[12] N. Fukuda *et al.*, Phys. Rev. C **70**, 054606 (2004).
[13] P. G. Hansen and B. Jonson, Europhys. Lett. **4**, 409 (1987).
[14] G. Bertsch and J. Foxwell, Phys. Rev. C **41**, 1300 (1990); **42**, 1159 (1990).
[15] Y. Suzuki and Y. Tosaka, Nucl. Phys. A **517**, 599 (1990).
[16] M. Honma and H. Sagawa, Prog. Theor. Phys. **84**, 494 (1990).
[17] G. F. Bertsch and H. Esbensen, Ann. Phys. **209**, 327 (1991).
[18] H. Sagawa, N. Takigawa, and N. van Giai, Nucl. Phys. A **543**, 575 (1992).
[19] A. Csoto, Phys. Rev. C **49**, 3035 (1994).
[20] T. Suzuki, H. Sagawa, and P. F. Bortignon, Nucl. Phys. A **662**, 282 (2000).
[21] E. Garrido, D. V. Fedorov, and A. S. Jensen, Nucl. Phys. A **708**, 277 (2002).
[22] T. Myo, S. Aoyama, K. Kato, and K. Ikeda, Phys. Lett. B **576**, 281 (2003).
[23] L. V. Chulkov *et al.*, Nucl. Phys. A **759**, 23 (2005).
[24] C. A. Bertulani and M. S. Hussein, Phys. Rev. C **76**, 051602 (2007).
[25] K. Hagino and H. Sagawa, Phys. Rev. C **76**, 047302 (2007).
[26] K. Hagino, H. Sagawa, T. Nakamura, and S. Shimoura, Phys. Rev. C **80**, 031301 (2009).
[27] D. Baye, P. Capel, P. Descouvemont, and Y. Suzuki, Phys. Rev. C **79**, 024607 (2009).
[28] Y. Kikuchi, K. Kato, T. Myo, M. Takashina, and K. Ikeda, Phys. Rev. C **81**, 044308 (2010).
[29] E. C. Pinilla, P. Descouvemont, and D. Baye, Phys. Rev. C **85**, 054610 (2012).
[30] Y. Kikuchi, T. Myo, K. Kato, and K. Ikeda, Phys. Rev. C **87**, 034606 (2013).
[31] T. Myo, A. Ohnishi, and K. Kato, Prog. Theor. Phys. **99**, 801 (1998).
[32] H. Sagawa, T. Suzuki, H. Iwasaki, and M. Ishihara, Phys. Rev. C **63**, 034310 (2001).
[33] M. Tohyama, Phys. Lett. B **323**, 257 (1994).
[34] I. Hamamoto, H. Sagawa, and X. Z. Zhang, Phys. Rev. C **53**, 765 (1996).
[35] I. Hamamoto and H. Sagawa, Phys. Rev. C **53**, R1492 (1996).
[36] H. Sagawa and T. Suzuki, Phys. Rev. C **59**, 3116 (1999).
[37] G. Colo and P. F. Bortignon, Nucl. Phys. A **696**, 427 (2001).
[38] T. Nakatsukasa and K. Yabana, Phys. Rev. C **71**, 024301 (2005).
[39] Y. Kanada-En'yo and M. Kimura, Phys. Rev. C **72**, 064301 (2005).

[40] P. Van Isacker, M. A. Nagarajan, and D. D. Warner, Phys. Rev. C **45**, R13 (1992).
[41] F. Catara, E. G. Lanza, M. A. Nagarajan, and A. Vitturi, Nucl. Phys. A **624**, 449 (1997).
[42] M. Matsuo, Nucl. Phys. A **696**, 371 (2001).
[43] D. Vretenar, N. Paar, P. Ring, and G. A. Lalazissis, Nucl. Phys. A **692**, 496 (2001).
[44] S. Goriely and E. Khan, Nucl. Phys. A **706**, 217 (2002).
[45] N. Paar, P. Ring, T. Niksic, and D. Vretenar, Phys. Rev. C **67**, 034312 (2003).
[46] N. Tsoneva, H. Lenske, and C. Stoyanov, Phys. Lett. B **586**, 213 (2004).
[47] M. Matsuo, K. Mizuyama, and Y. Serizawa, Phys. Rev. C **71**, 064326 (2005).
[48] J. Piekarewicz, Phys. Rev. C **73**, 044325 (2006).
[49] J. Terasaki and J. Engel, Phys. Rev. C **74**, 044301 (2006).
[50] J. Liang, L. G. Cao, and Z. Y. Ma, Phys. Rev. C **75**, 054320 (2007).
[51] N. Tsoneva and H. Lenske, Phys. Rev. C **77**, 024321 (2008).
[52] N. Paar, D. Vretenar, E. Khan, and G. Colo, Rep. Prog. Phys. **70**, 691 (2007).
[53] K. Yoshida and N. V. Giai, Phys. Rev. C **78**, 014305 (2008).
[54] G. Co', V. De Donno, C. Maieron, M. Anguiano, and A. M. Lallena, Phys. Rev. C **80**, 014308 (2009).
[55] M. Martini, S. Peru, and M. Dupuis, Phys. Rev. C **83**, 034309 (2011).
[56] T. Inakura, T. Nakatsukasa, and K. Yabana, Phys. Rev. C **84**, 021302 (2011).
[57] X. Roca-Maza, G. Pozzi, M. Brenna, K. Mizuyama, and G. Colo, Phys. Rev. C **85**, 024601 (2012).
[58] S. Ebata, T. Nakatsukasa, and T. Inakura, Phys. Rev. C **90**, 024303 (2014).
[59] S. Bacca, N. Barnea, G. Hagen, M. Miorelli, G. Orlandini, and T. Papenbrock, Phys. Rev. C **90**, 064619 (2014).
[60] J. Piekarewicz, Phys. Rev. C **83**, 034319 (2011).
[61] A. Carbone, G. Colo, A. Bracco, L. G. Cao, P. F. Bortignon, F. Camera, and O. Wieland, Phys. Rev. C **81**, 041301 (2010).
[62] P.-G. Reinhard and W. Nazarewicz, Phys. Rev. C **87**, 014324 (2013).
[63] T. Inakura, T. Nakatsukasa, and K. Yabana, Phys. Rev. C **88**, 051305 (2013).
[64] K. Govaert, F. Bauwens, J. Bryssinck, D. De Frenne, E. Jacobs, W. Mondelaers, L. Govor, and V. Y. Ponomarev, Phys. Rev. C **57**, 2229 (1998).
[65] R.-D. Herzberg *et al.*, Phys. Rev. C **60**, 051307(R) (1999).
[66] A. Leistenschneider *et al.*, Phys. Rev. Lett. **86**, 5442 (2001).
[67] N. Ryezayeva *et al.*, Phys. Rev. Lett. **89**, 272502 (2002).
[68] E. Tryggestad *et al.*, Phys. Rev. C **67**, 064309 (2003).
[69] T. Hartmann, M. Babilon, S. Kamerdzhiev, E. Litvinova, D. Savran, S. Volz, and A. Zilges, Phys. Rev. Lett. **93**, 192501 (2004).
[70] P. Adrich *et al.*, Phys. Rev. Lett. **95**, 132501 (2005).
[71] J. Gibelin *et al.*, Phys. Rev. Lett. **101**, 212503 (2008).
[72] A. Klimkiewicz *et al.*, Phys. Rev. C **76**, 051603(R) (2007).
[73] R. Schwengner *et al.*, Phys. Rev. C **78**, 064314 (2008).
[74] O. Wieland *et al.*, Phys. Rev. Lett. **102**, 092502 (2009).
[75] J. Endres, D. Savran, A. M. van den Berg, P. Dendooven, M. Fritzsche, M. N. Harakeh, J. Hasper, H. J. Wörtche, and A. Zilges, Phys. Rev. C **80**, 034302 (2009).
[76] J. Endres *et al.*, Phys. Rev. Lett. **105**, 212503 (2010).
[77] A. Tamii *et al.*, Phys. Rev. Lett. **107**, 062502 (2011).
[78] B. L. Berman and S. C. Fultz, Rev. Mod. Phys. **47**, 713 (1975).
[79] M. J. Jakobson, Phys. Rev. **123**, 229 (1961).
[80] R. J. Hughes, R. H. Sambell, E. G. Muirhead, and B. M. Spicer, Nucl. Phys. A **238**, 189 (1975).
[81] A. M. Goryachev, G. N. Zalesnyy, and I. V. Pozdnev, Izv. Ross. Akad. Nauk, Ser. Fiz. **56**, 159 (1992).
[82] H. Utsunomiya, Y. Yonezawa, H. Akimune, T. Yamagata, M. Ohta, M. Fujishiro, H. Toyokawa, and H. Ohgaki, Phys. Rev. C **63**, 018801 (2000).
[83] C. W. Arnold, T. B. Clegg, C. Iliadis, H. J. Karwowski, G. C. Rich, J. R. Tompkins, and C. R. Howell, Phys. Rev. C **85**, 044605 (2012).
[84] H. Ustunomiya *et al.*, Phys. Rev. C **92**, 064323 (2015).
[85] J. Ahrens *et al.*, Nucl. Phys. A **251**, 479 (1975).
[86] S. Okabe, Y. Abe, and H. Tanaka, Prog. Theor. Phys. **57**, 866 (1977).
[87] S. Okabe and Y. Abe, Prog. Theor. Phys. **59**, 315 (1978).
[88] A. C. Fonseca, J. Revai, and A. Matveenko, Nucl. Phys. A **326**, 182 (1979).
[89] P. Descouvemont, Phys. Rev. C **39**, 1557 (1989).
[90] K. Arai, Y. Ogawa, Y. Suzuki, and K. Varga, Phys. Rev. C **54**, 132 (1996).
[91] V. D. Efros and J. M. Bang, Eur. Phys. J. A **4**, 33 (1999).
[92] K. Arai, P. Descouvemont, D. Baye, and W. N. Catford, Phys. Rev. C **68**, 014310 (2003).
[93] O. Burda, P. von Neumann-Cosel, A. Richter, C. Forssen, and B. A. Brown, Phys. Rev. C **82**, 015808 (2010).
[94] E. Garrido, D. V. Fedorov, and A. S. Jensen, Phys. Lett. B **684**, 132 (2010).
[95] R. Alvarez-Rodriguez, A. S. Jensen, E. Garrido, and D. V. Fedorov, Phys. Rev. C **82**, 034001 (2010).
[96] V. D. Efros, P. von Neumann-Cosel, and A. Richter (European Centre for Theoretical Studies in Nuclear Physics and Related Areas Collaboration), Phys. Rev. C **89**, 027301 (2014).
[97] M. Odsuren, Y. Kikuchi, T. Myo, M. Aikawa, and K. Kato, Phys. Rev. C **92**, 014322 (2015).
[98] A. Ono, H. Horiuchi, T. Maruyama, and A. Ohnishi, Phys. Rev. Lett. **68**, 2898 (1992).
[99] A. Ono, H. Horiuchi, T. Maruyama, and A. Ohnishi, Prog. Theor. Phys. **87**, 1185 (1992).
[100] Y. Kanada-En'yo, H. Horiuchi, and A. Ono, Phys. Rev. C **52**, 628 (1995).
[101] Y. Kanada-En'yo and H. Horiuchi, Phys. Rev. C **52**, 647 (1995).
[102] Y. Kanada-En'yo and H. Horiuchi, Prog. Theor. Phys. Suppl. **142**, 205 (2001).
[103] Y. Kanada-En'yo, M. Kimura, and A. Ono, Prog. Theor. Exp. Phys. **2012**, 01A202 (2012).
[104] T. Furuta, K. H. O. Hasnaoui, F. Gulminelli, C. Leclercq, and A. Ono, Phys. Rev. C **82**, 034307 (2010).
[105] Y. Kanada-En'yo, Phys. Rev. Lett. **81**, 5291 (1998).
[106] Y. Kanada-En'yo, H. Horiuchi, and A. Dote, Phys. Rev. C **60**, 064304 (1999).
[107] Y. Kanada-En'yo, Prog. Theor. Phys. **117**, 655 (2007); **121**, 895 (2009).
[108] Y. Kanada-En'yo, Phys. Rev. C **89**, 024302 (2014).
[109] H. Feldmeier, K. Bieler, and J. Schnack, Nucl. Phys. A **586**, 493 (1995).

[110] T. Neff and H. Feldmeier, Nucl. Phys. A **713**, 311 (2003).
[111] T. Ando, K. Ikeda, and A. Tohsaki, Prog. Theor. Phys. **64**, 1608 (1980).
[112] R. Tamagaki, Prog. Theor. Phys. **39**, 91 (1968).
[113] N. Yamaguchi, T. Kasahara, S. Nagata, and Y. Akaishi, Prog. Theor. Phys. **62**, 1018 (1979).
[114] M. Seya, M. Kohno, and S. Nagata, Prog. Theor. Phys. **65**, 204 (1981).
[115] W. von Oertzen, Z. Phys. A **354**, 37 (1996); **357**, 355 (1997).
[116] F. Ajzenberg-Selove, Nucl. Phys. A **490**, 1 (1988).
[117] D. R. Tilley, J. H. Kelley, J. L. Godwin, D. J. Millener, J. E. Purcell, C. G. Sheu, and H. R. Weller, Nucl. Phys. A **745**, 155 (2004).